Journal of Luminescence 280 (2025) 121091

Contents lists available at ScienceDirect

Journal of Luminescence

journal homepage: www.elsevier.com/locate/jlumin

Full Length Article

On the luminescent properties of Eu^{3+} doped $La_2Hf_3(WO_4)_9$

Julia Goldmann *, Tim Pier, Thomas Jüstel

FH Münster University of Applied Sciences, Stegerwaldstr. 39, D-48565, Steinfurt, Germany

ARTICLE INFO

Keywords:
Europium
Photoluminescence
X-ray luminescence
Time dependent spectroscopy
Tungstates

ABSTRACT

This work concerns the host material $La_2Hf_3(WO_4)_9$ doped with Eu^{3+} as a widely applied red emitting activator, focusing on its luminescent properties under various excitation conditions. $La_{2\text{-}x}Eu_xHf_3(WO_4)_9$ solid solutions were synthesized and confirmed to crystallize in a single-phase structure. The reflectivity decreases with increasing Eu^{3+} doping level, while characteristic Eu^{3+} electronic transitions emerge, enhancing absorption strength and emission intensity. Emission spectra under various excitation conditions (395 nm; 160 nm; X-rays) reveal concentration-dependent characteristic Eu^{3+} luminescence behavior with stable peak positions and red emission profiles. Under X-ray excitation, luminescence peaks at 10 % Eu^{3+} doping, followed by intensity quenching at higher concentrations due to non-radiative mechanisms. The depth of X-ray penetration, calculated using the Feldman equation, correlates with the observed luminescence efficiency. The materials exhibit a rather low thermal quenching temperature, with $T_{1/2}$ determined as 228 K. Lifetime measurements highlight concentration quenching effects and distinct Eu^{3+} environments. Chromaticity coordinates confirm a consistent red emission with minor variations across doping levels. The study provides insights into the structural, optical, and thermal properties of Eu^{3+}-doped $La_2Hf_3(WO_4)_9$, emphasizing its potential and limitations for luminescent applications.

1. Introduction

In the second half of the 20th century, researchers in industry and academia discovered that Eu^{3+} is a very efficient and long-term stable activator ion, which can accommodate high concentrations in many hosts before concentration quenching occur. This led to the development of several Eu^{3+} activated red emitter based on hosts such as oxides, oxysulphides, borates, phosphates, vanadates and so on, for light sources, displays, and other photonic technologies [1]. This research inspired extensive studies into materials like Eu^{3+} [2]. For example, it turned out that Eu^{3+} and Tb^{3+} co-doped tungstates or molybdates show good suitability for application in full color displays, light-emitting devices or as a multifunctional luminescent thermometer [3,4]. Red emitting phosphors, in particular, play a crucial role in achieving balanced white light by improving the color rendering index (CRI) and creating a more pleasing correlated color temperature (CCT), particularly for indoor illumination, even if they decrease somewhat the luminous efficacy [5–7]. Eu^{3+} has emerged as a leading dopant for red phosphors due to its sharp and intense emission in the red spectral range, resulting in red light with a high color saturation. The electronic structure of Eu^{3+}, with an even number of 4f electrons, interacts with the crystalline host matrix, allowing the crystal-field effects to partially or fully remove the degeneracies of its $^{2S+1}L_J$ levels. Compared to other lanthanide ions with even numbers of 4f electrons, Eu^{3+} offers a distinct advantage: the starting levels for its transitions in both absorption and luminescence spectra are non-degenerate ($J = 0$). Moreover, its small total angular momentum (J) simplifies spectral analysis [8]. By analyzing the number of emission lines from the $^5D_0 \rightarrow {}^7F_J$ transitions in the luminescence spectrum and the $^5D_J \rightarrow {}^7F_0$ transitions in the absorption spectrum, the symmetry of the Eu^{3+} site in the host lattice can be determined. These features have solidified Eu^{3+} as another widely used red-emitting activator in fluorescent lamps, emissive displays, and related technologies [9,10]. Introducing red emission into lighting systems inherently reduces luminous efficacy due to the human eye's low sensitivity in the red spectral range. Warm white light sources often rely on broadband red emitters like $(Sr,Ba)_2Si_5N_8:Eu^{2+}$ and $(Ca,Sr)AlSiN_3:Eu^{2+}$. While these phosphors are highly efficient, their emissions extend into the deep red region beyond 700 nm, where human eye sensitivity drops almost to zero, leading to a relatively low luminous efficacy [11,12]. In contrast, narrow-band emitters such as Mn^{4+} and line emitters like Sm^{3+} or Eu^{3+} provide significantly higher luminous efficacy (LE) while still supporting a high CRI. For example, employing Eu^{3+}

---

* Corresponding author.
E-mail address: julia.exeler@fh-muenster.de (J. Goldmann).

https://doi.org/10.1016/j.jlumin.2025.121091
Received 19 December 2024; Received in revised form 9 January 2025; Accepted 16 January 2025

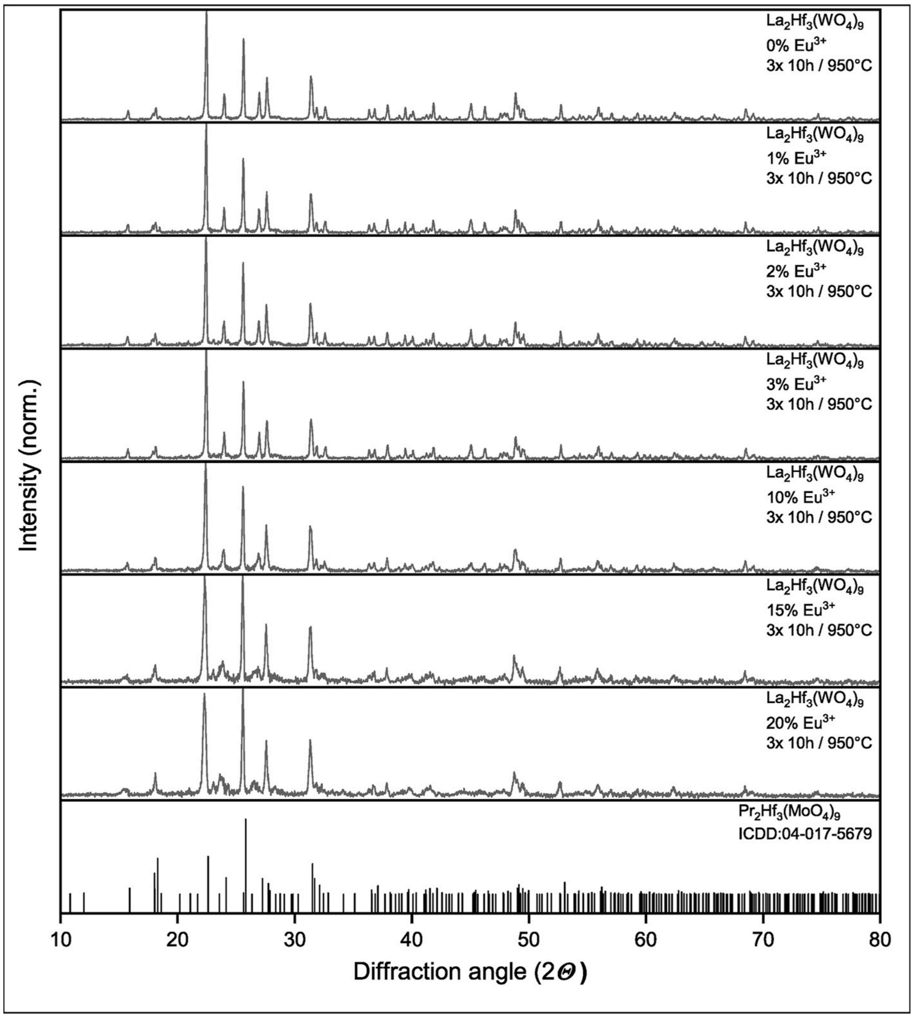

Fig. 1. XRD patterns of $La_2Hf_3(WO_4)_9$ upon Cu K_{alpha} radiation.

activated phosphors in warm white pcLEDs can lead to high LE and good CRI values. $(Tb_{0,8}Eu_{0,2})_2Mo_3O_{12}$ shows great potential as a radiation converter for producing warm-white pcLEDs with high efficiency and a good CRI [13]. Other well-known red-emitting phosphors are Y_2O_3:Eu^{3+}, (Y,Gd)BO_3:Eu^{3+}, YVO_4:Eu^{3+}, Y_2O_2S:Eu^{3+} and Y(P,V)O_4:Eu^{3+} which produce intense red emission under UV excitation [14–19]. Equivalent to the related molybdate compounds $Ln_2Zr_3(MoO_4)_9$ (Ln = La-Gd) and $Ln_2Hf_3(MoO_4)_9$ (Ln = La-Lu, Y, Sc), $La_2Hf_3(WO_4)_9$ crystallizes in the trigonal crystal system with space group R-3c (167) [20–26]. Despite its potential, detailed studies on the luminescent behavior of Eu^{3+} in the $La_2Hf_3(WO_4)_9$ host lattice remain sparse. In this study, Eu^{3+}-doped $La_2Hf_3(WO_4)_9$ was synthesized and its luminescent properties were investigated. Our focus is on understanding the structural compatibility of this host with Eu^{3+}, the energy transfer mechanisms, and the emission characteristics under various excitation conditions. By exploring the interplay between the crystal lattice and the dopant ions, we aim to provide insights into the design of advanced luminescent materials that combine efficiency, stability, and application versatility.

2. Experimental section

Microscale powder samples of $La_{2-x}Eu_xHf_3(WO_4)_9$ with 0 %, 1 %, 2 %, 3 %, 10 %, 15 % and 20 % Eu^{3+} were prepared by solid-state synthesis method. The starting materials were stochiometric amounts of high purity La_2O_3 (99.99 %, Treibacher Industrie AG), HfO_2 (Aldrich), MoO_3 (99.9 %, Alfa Aesar) and Eu_2O_3 (99.99 %, Treibacher Industrie AG). The mixture was thoroughly mixed in an agate mortar with added ethanol as grinding medium. After drying, the mixtures were transferred to alumina crucibles and calcined in air three times at 1223 K for 10 h. X-Ray diffraction (XRD) analysis was performed by using a RIGAKU MiniFlex II and reflection spectra upon using an Edinburgh Instruments FLS 920 spectrometer against $BaSO_4$ as a white powder reference. Photoluminescence, i.e. emission and excitation spectra were recorded by using an Edinburgh Instruments FLS 920 spectrometer with a 450 W Xe discharge lamp. Moreover, the x-ray excited emission spectra were taken by using a modified Edinburgh Instruments FLS 980 spectrometer equipped with an Oxford Instruments Neptune 5200 Series X-Ray tube. Finally, emission spectra excited by VUV radiation by using a modified Edinburgh Instruments FLS 920 spectrometer with a deuterium lamp (DS-775-100, Hamamatsu) and a VUV monochromator, which was evacuated by turbo molecular pump, were performed.

3. Results and discussion

The XRD patterns of the synthesized powders, as shown in Fig. 1, confirm that single-phase materials were successfully obtained across all Eu^{3+} concentrations. This conforms that all $La_{2-x}Eu_xHf_3(WO_4)_9$ samples crystallize in the same structure type, i.e. a solid solution without a miscibility gap is observed, which is not surprising as the ionic radii of La^{3+} and Eu^{3+} differ by only about 7 %. This small difference allows Vegard's law to be applied, suggesting the formation of a complete solid solution series with a linear relationship between the host lattice

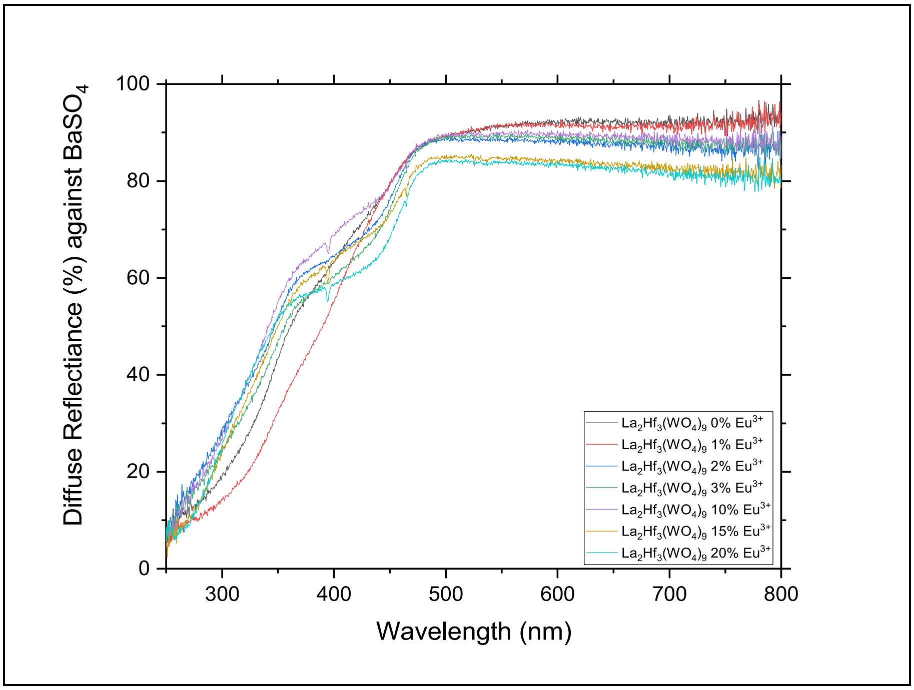

Fig. 2. Diffuse reflection spectra of the $La_2Hf_3(WO_4)_9$ samples doped with 0, 1, 2, 3, 10, 15, or 20 % Eu^{3+}.

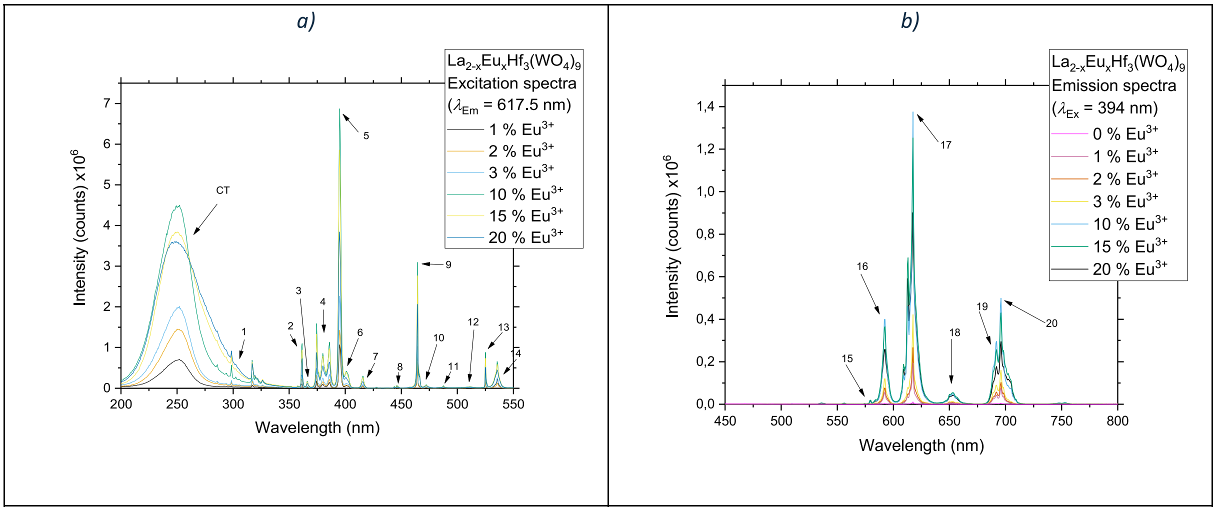

Fig. 3. a) Excitation spectra of $La_{2\text{-}x}Eu_xHf_3(WO_4)_9$ b) Emission spectra of $La_{2\text{-}x}Eu_xHf_3(WO_4)_9$.

constants and the La^{3+}/Eu^{3+} ratio [27]. W^{6+} and Mo^{6+} exhibit similar ionic radii (Mo^{6+}: 59 p.m., CN = 6; W^{6+}: 60 p.m., CN = 6) due to the effects of lanthanide contraction. This similarity in size leads to comparable chemical behavior, and they often form analogous structures. In fact, several studies have successfully synthesized solid solutions incorporating both materials [28–31]. Since Hf^{4+} and Zr^{4+} also have nearly identical ionic radii and the same charge, it can be assumed that $La_2Hf_3(WO_4)_9$ is isostructural with $Ln_2Hf_3(MoO_4)_9$ and $La_2Zr_3(MoO_4)_9$. Therefore, those structural descriptions are used for the $La_{2\text{-}x}Eu_xHf_3(WO_4)_9$ powder samples synthesized in this work [26,32,33].

Fig. 2 summarizes the reflection spectra of undoped and Eu3+ doped $La_2Hf_3(WO_4)_9$. The broad absorption band (250–470 nm) observed in the samples is attributed to band-to-band transitions. In oxides, the top of the valence band is primarily composed of O^{2-} 2p states. In $La_2Hf_3(WO_4)_9$, the bottom of the conduction band is likely formed by the empty 4d states of Hf^{4+} and W^{6+}, with the addition of empty 5d states of Eu^{3+} at higher energies in the doped samples. These direct band-to-band transitions conserve electron momentum, resulting in a high transition probability and strong absorption. From a localized perspective, these transitions are often referred to as charge transfer (CT) transitions, or more specifically, ligand-to-metal charge transfer (LMCT), as they involve the transfer of electron density from the ligand to the metal. Since the electron configuration of the excited CT state differs significantly from that of the ground state, these transitions are associated with a large Stokes shift. This large shift often results in CT luminescence exhibiting low thermal stability [34]. The reflectivity of the samples decreased significantly as the concentration of doped Eu^{3+} increased. For the undoped sample, the reflectance was 95 %, but it dropped to approximately 80 % for the sample with 20 % Eu^{3+}. This indicates that doping with Eu^{3+} enhances the absorption strength. Additionally, sharp peaks began to emerge when the Eu^{3+} concentration exceeded 5 %, specifically at 395.5 nm and 465.5 nm. These peaks correspond to the

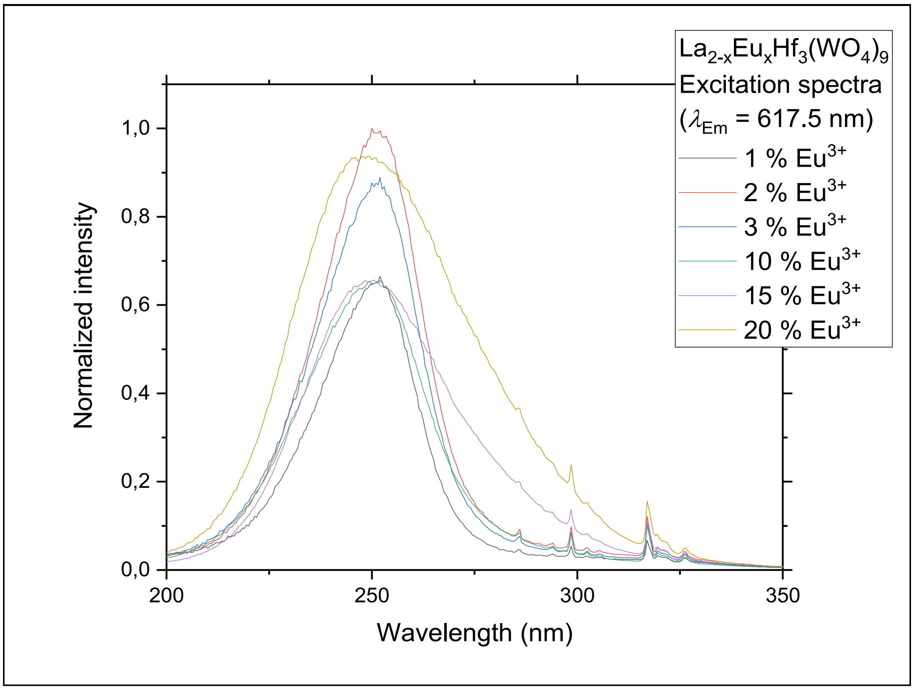

Fig. 4. UV region of the normalized excitation spectra of $La_2Hf_3(MoO_4)_9$ with 1–20 % Eu^{3+} monitored at 617.5 nm.

Table 1
Eu^{3+} intraconfigurational 4f-4f transitions with their respective peak wavelength or range, peak wavenumber or range and assigned number for reference in this work.

Number	Wavelength [nm][a]	Wavenumber [x 10^3 cm^{-1}][b]	Transitions
1	~298–330	~30.3–33.5	$^7F_0 \rightarrow {}^5H_J$ (J = 3 … 7)
2	361.5	27.7	$^7F_0 \rightarrow {}^5D_4$
3	366.2	27.3	$^7F_1 \rightarrow {}^5D_4$
4	~374.5–386	~25.9–26.7	$^7F_0 \rightarrow {}^5L_8 + {}^5G_J + {}^5L_9 + {}^5L_{10}$ (J = 2 … 6)
5	394	25.3	$^7F_0 \rightarrow {}^5L_7$
6	~400–404	~24.8–25.9	$^7F_0 \rightarrow {}^5L_6$
7	416	24.0	$^7F_1 \rightarrow {}^5D_3$
8	446	22.5	$^7F_3 \rightarrow {}^5D_3$
9	465	21.5	$^7F_0 \rightarrow {}^5D_2$
10	472	21.1	$^7F_1 \rightarrow {}^5D_2$
11	488	20.5	$^7F_2 \rightarrow {}^5D_2$
12	~510–513	~19.5-16.9	$^7F_3 \rightarrow {}^5D_2$
13	525	19.0	$^7F_0 \rightarrow {}^5D_1$
14	535.5	18.6	$^7F_1 \rightarrow {}^5D_1$
15	579	17.3	$^5D_0 \rightarrow {}^7F_0$
16	592.5	16.9	$^5D_0 \rightarrow {}^7F_1$
17	~609–617.5	~16.3-16.4	$^5D_0 \rightarrow {}^7F_2$
18	~648–658	~15.2-15.5	$^5D_0 \rightarrow {}^7F_3$
19	691	14.5	$^5D_0 \rightarrow {}^7F_4$
20	696	14.4	$^5D_0 \rightarrow {}^7F_5$

[a] Transitions 1–14 were determined from excitation spectra, transitions 15–20 were determined from emission spectra.
[b] Calculated from the experimentally determined wavelengths.

$^7F_0 \rightarrow {}^5L_6$ and $^7F_0 \rightarrow {}^5D_2$ electronic transitions, respectively [35]. For a more in-depth investigation of the luminescence properties of $La_2Hf_3(WO_4)_9$, emission and excitation spectra were examined. Not all samples show a systematic change as the 10 % shows a higher reflection as the 1 % sample. This could be attributed to unreacted WO_3. It seems that although the XRD looks clean, traces of it can still be seen in the reflection spectra. This could lead to the inconsistent shape.

Excitation spectra of $La_2Hf_3(WO_4)_9$:Eu^{3+} (Eu^{3+} = 1 %, 2 %, 3 %, 10 %, 15 %, 20 %) for the 617.5 nm emission ($^5D_0 \rightarrow {}^7F_2$) are shown in Fig. 3a). In the UV range from 200 to 350 nm, a broad, structured band is observed. For a closer look at the CT band, the spectrum was normalized to compensate for the increasing emission intensity with rising Eu^{3+} concentration (Fig. 4).

It can be observed that the shape of the excitation band changes significantly with increasing Eu^{3+} concentration. The broadening of the CT band with increasing Eu^{3+} concentration can be attributed to the contributions of the appearance of the O^{2-} to Eu^{3+} LMCT. At low Eu^{3+} concentration, the CT band is dominated by the O^{2-} to W^{6+} LMCT, which appears as a narrower feature in the excitation spectrum. As the Eu^{3+} content rises, the O^{2-}/Eu^{3+} LMCT band becomes more prominent, leading to the observed broadening. Similarly, to the molybdates, the O^{2-} to MoO^{6+} LMCT also exhibits a lower quantum yield. In contrast, the quantum yield of the O^{2-}/Eu^{3+} LMCT is generally very high, which also appears to apply to the tungstates [36–39]. The sharp lines observed in the excitation spectra can be attributed to Eu^{3+} intraconfigurational transitions of the type $[Xe]4f^6 \rightarrow [Xe]4f^6$ (Table 1). Most of these lines originate from transitions starting in the $^7F_0$ ground state. However, transitions 3, 7, 8, 10, 11, 12, and 14 originate from excited states $^7F_1$, $^7F_2$ and $^7F_3$. By comparing the positions of the $^7F_0 \rightarrow {}^5D_4$ and $^7F_1 \rightarrow {}^5D_4$ transitions (labeled as number 2 and 3), which occur at approximately $27.7x10^3$ cm^{-1} and $27.3x10^3$ cm^{-1}, it can be deduced that the $^7F_1$ state lies about 400 cm^{-1} above $^7F_0$. A similar comparison of the $^7F_0 \rightarrow {}^5D_2$ and $^7F_1 \rightarrow {}^5D_2$ transitions ($21.5x10^3$ cm^{-1} and $21.1x10^3$ cm^{-1}) as well as the $^7F_0 \rightarrow {}^5D_1$ and $^7F_1 \rightarrow {}^5D_1$ transitions ($19.0x10^3$ cm^{-1} and $18.6x10^3$ cm^{-1}) confirm the same energy difference of approximately 400 cm^{-1}. A similar analysis for the $^7F_2$ and $^7F_3$ levels reveals energy separations of approximately $1x10^3$ cm^{-1} ($^7F_2$) and $2x10^3$ cm^{-1} ($^7F_3$) from the ground state $^7F_0$ [33].

Under 394 nm excitation, $La_2Hf_3(WO_4)_9$:Eu^{3+} (Eu^{3+} = 1 %, 2 %, 3 %, 10 %, 15 %, 20 %) shows an emission spectrum consisting of several narrow lines (Fig. 3b). The lines can be assigned to the respective transitions based on the numbers in the figure using Table 1. The emission spectrum is dominated by lines with maxima at 592.5 nm, 617.5 nm and 696 nm. These lines are typically the most intense and are each based on a transition from the excited $^5D_0$ state to the $^7F_1$, $^7F_2$ and $^7F_5$ states. The other observed lines are based on transitions starting from $^5D_1$, $^5D_2$ or $^5D_3$ states. The intensity of these lines is significantly lower than that of the $^5D_0$ lines. The reason for that is that the $^5D_1$, $^5D_2$

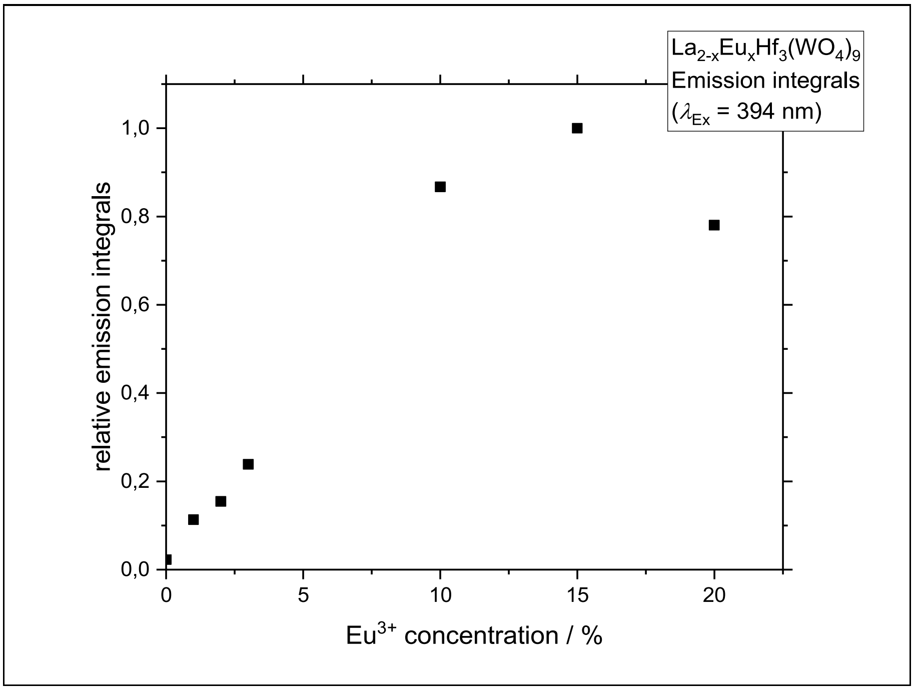

Fig. 5. Relative emission integrals depending on the Eu^{3+} concentration in $La_{2-x}Eu_xHf_3(WO_4)_9$ under 394 nm excitation.

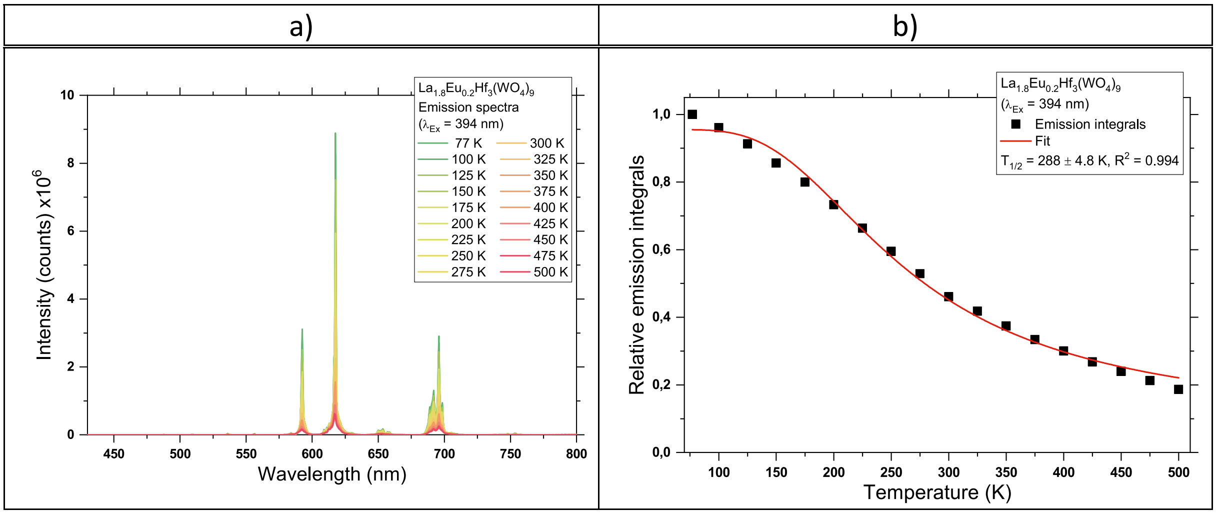

Fig. 6. a) Temperature dependent emission spectra of $La_{1.8}Eu_{0.2}Hf_3(WO_4)_9$ b) Integrated emission intensity of different temperature.

and $^5D_3$ are emptied by radiationless transitions to the $^5D_0$ state with the formation of phonons [40–43].

The emission intensity increases steadily as the Eu^{3+} concentration rises, reaching a peak at 15 % doping. This trend occurs because more Eu^{3+} ions are available to absorb and emit energy, enhancing the overall luminescence. At concentrations beyond 15 %, concentration quenching becomes significant (Fig. 5). The close proximity of Eu^{3+} ions facilitates non-radiative energy transfer mechanisms such as cross-relaxation and energy migration, which dissipate energy as heat rather than light. These processes result in a decline in emission efficiency, limiting the effectiveness of higher Eu^{3+} doping levels for luminescent applications.

The thermal quenching behavior of $La_{1.8}Eu_{0.2}Hf_3(WO_4)_9$ was examined by recording temperature resolved emission spectra under 394 nm excitation. The best performance w.r.t. excitation spectra at 617.5 nm emission and emission spectra upon 394 nm excitation can be found for the sample doped by 10 % Eu^{3+}, even though the 15 % sample shows an overall better emission intensity. As shown in Fig. 6 a) the emission intensity systematically decreased with rising temperature, while the peak positions remained unchanged. The integrated emission intensity over temperature is presented in Fig. 6 b) and was analyzed using a modified Fermi–Dirac function, yielding a quenching temperature $T_{1/2} = 228 \pm 4.8$ K with an excellent fit ($R^2 = 0.994$) [44].

$$f(E) = \frac{1}{1 + e^{\frac{(E-E_F)}{kT}}}$$

where E_F is the Fermi energy.

This relatively low thermal quenching temperature indicates that the material is unsuitable for applications requiring thermal stability. The pronounced non-radiative relaxation can be attributed to the larger distance (ΔR) between the metal ions and ligand groups in the excited and ground states. A greater ΔR facilitates non-radiative processes, leading to reduced emission efficiency. Factors influencing ΔR include

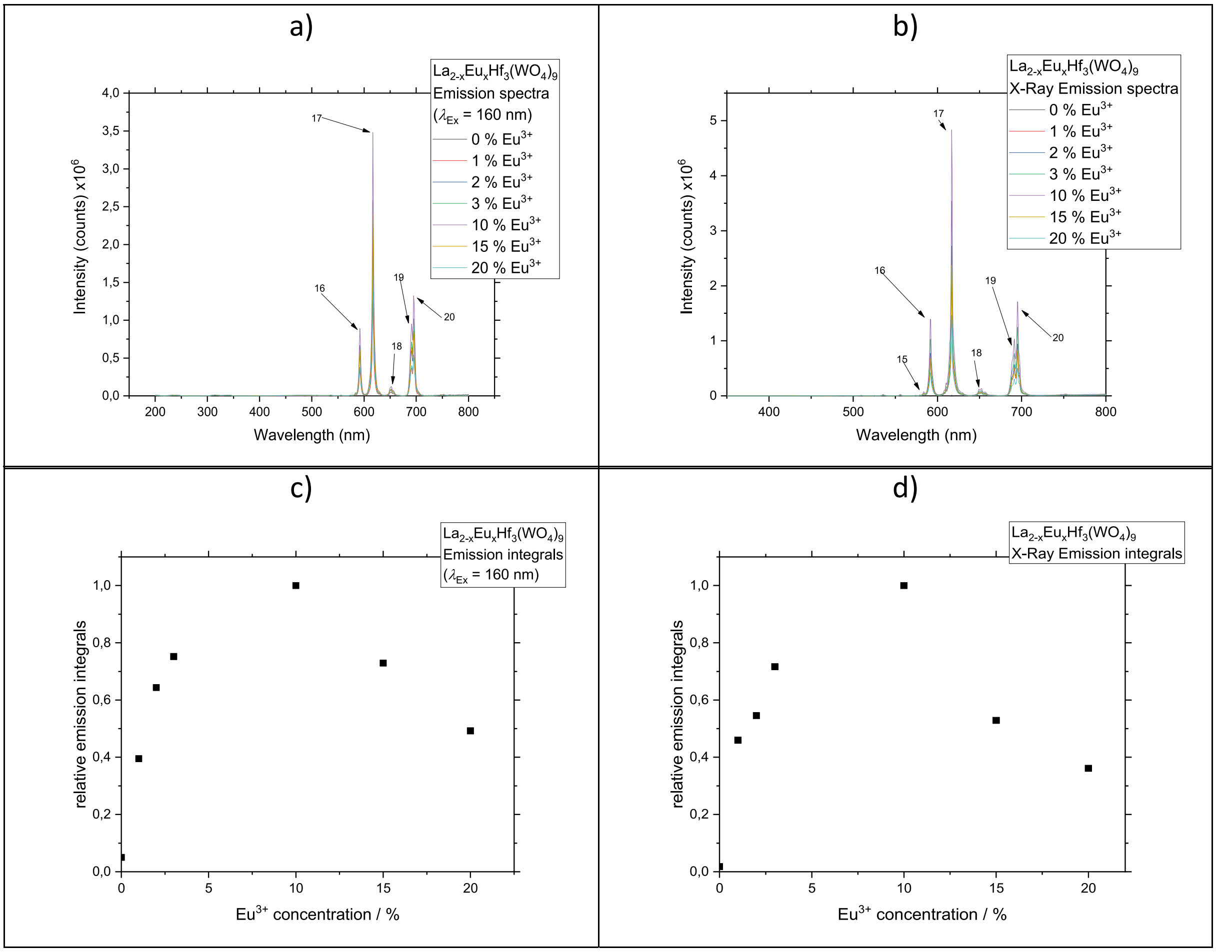

Fig. 7. a) VUV emission spectra of $La_2Hf_3(WO_4)_9$ with 0–20 % Eu^{3+} b) X-Ray excited emission spectra of $La_2Hf_3(WO_4)_9$ with 0–20 % Eu^{3+} c) Relative emission integrals depending on the Eu^{3+} concentration in $La_{2-x}Eu_xHf_3(WO_4)_9$ under 160 nm excitation d) Relative emission integrals depending on the Eu^{3+} concentration in $La_{2-x}Eu_xHf_3(WO_4)_9$ under X-Ray.

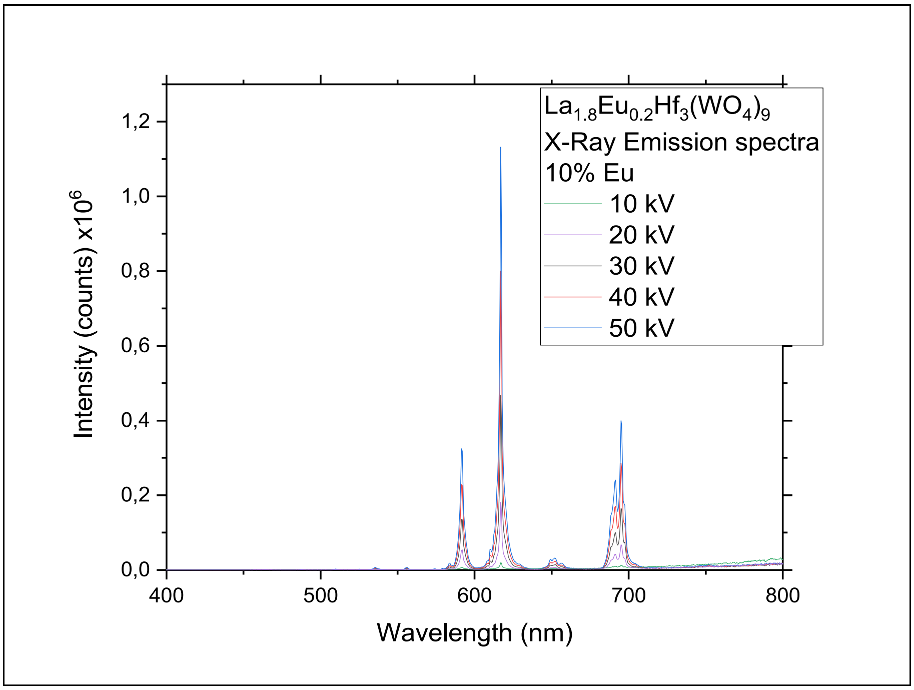

Fig. 8. X-Ray emission spectra of $La_{1.8}Eu_{0.2}Hf_3(WO_4)_9$ upon varying excitation voltages.

Table 2
Calculated approximate values for X-Ray penetration depths P_d.

Excitation energy [keV]	P_d [Å]	P_d [nm]
10	219.23	21.9
20	895.41	89.5
30	2039.08	203.9
40	3656.15	365.6
50	5750.74	575.1

the size and charge of the cations surrounding the activator as well as the lattice environment altered by the substitution of the host cation with Eu^{3+} [45].

Fig. 7a) presents the emission spectra of $La_{2-x}Eu_xHf_3(WO_4)_9$ samples under VUV excitation ($\lambda_{ex} = 160$ nm), recorded between 150 nm 850 nm. The spectra display the characteristic Eu^{3+} transitions listed in Table 1. Notably, the $^5D_0 \rightarrow {}^7F_0$ transition (15) is absent, despite the significantly higher emission intensity compared to the spectra under 394 nm excitation. Fig. 7b) illustrates the emission spectra of the samples under X-Ray excitation (50 kV, 1.7 mA), which were recorded between 350 nm and 800 nm. The spectra also exhibit the typical Eu^{3+} transitions shown in Table 1 with no noticeable differences from the emission spectra under 394 nm excitation, apart from a notably stronger overall emission intensity. By comparing the relative emission integrals of Fig. 7c) and d) with those in Fig. 5, it becomes apparent that the emission intensity peaks at 10 % Eu^{3+} concentration under VUV and X-Ray excitation. This behavior could be attributed to faster quenching mechanisms, as VUV and X-Ray excitation directly excite the host lattice, rather than the Eu^{3+} 4f-4f transitions. Consequently, less energy is effectively transferred to the Eu^{3+} ions, limiting the overall emission efficiency.

Under 10 kV X-ray excitation, $La_{1.8}Eu_{0.2}Hf_3(WO_4)_9$ exhibits a significant reduction in luminescence intensity, with only faint emission observed. Despite the drastic drop in intensity, the emission peak positions remain consistent across excitation voltages of 10 kV, 20 kV, 30 kV, 40 kV, and 50 kV (Fig. 8). This suggests that the spectral characteristics of the Eu^{3+} transitions are not affected by the varying excitation energies, but the overall efficiency of energy transfer to the emitting Eu^{3+} centers is substantially diminished at lower excitation voltages. To calculate the penetration depths P_d for electron impingement the Feldman equation is used [46].

$$P_d = \frac{250}{\rho Z^{n/2}} U^n \text{ with } n = \frac{1.2}{1 - 0.29 \log_{10} Z}$$

U = energy of electrons in keV; Z = atomic number; ρ = density of the material

For the density, the density of $La_2Hf_3(MoO_4)_9$ ($\rho = 4.53$ g/cm^3) was taken as an approximation [26]. The atomic number Z was calculated as follows:

$$Z = \frac{\text{Sum of atomic numbers weighted by their counts}}{\text{Total number of atoms in the formula}}$$

Thus, Z for $La_2Hf_3(WO_4)_9$ is approximately 25.68.

In order to obtain a better visualization of the values seen in Table 2, they are portrayed in Fig. 9. The penetration depth values are fairly close to the linear trend, as shown by the high R^2 value of 0.96065. The slight deviations from perfect linearity can be attributed to approximations inherent in the calculation method. At 10 kV, the penetration depth is minimal, resulting in the weak luminescence observed above.

The presence of two decay constants τ_1 and τ_2 indicates that the luminescent decay is influenced by multiple processes rather than a single exponential behavior (Fig. 10). A monoexponential fit was attempted but did not provide an acceptable fit to the experimental data. The Eu^{3+} ions occupy a single crystallographic environment in this material. Instead of distinct emitting species, the biexponential decay could be attributed to energy migration among the Eu^{3+} ions, an inhomogeneous distribution of dopants, clustering of Eu^{3+} ions at the particle surfaces or exchange interactions. These effects could create regions with differing dynamics which manifest as separate decay components. The shorter lifetime τ_1 decreases with increasing Eu^{3+} concentration from 586.41 μs at 1 % Eu^{3+} to 495.29 μs at 20 % Eu^{3+}. This trend suggests increasing concentration quenching, where energy transfer between closely spaced Eu^{3+} ions leads to non-radiative decay processes. This behavior is typical for high doping levels, where ion-ion interactions become significant. The longer lifetime τ_2 exhibits a less pronounced decrease, from 1657.32 μs at 1 % Eu^{3+} to 1491.27 μs at 20

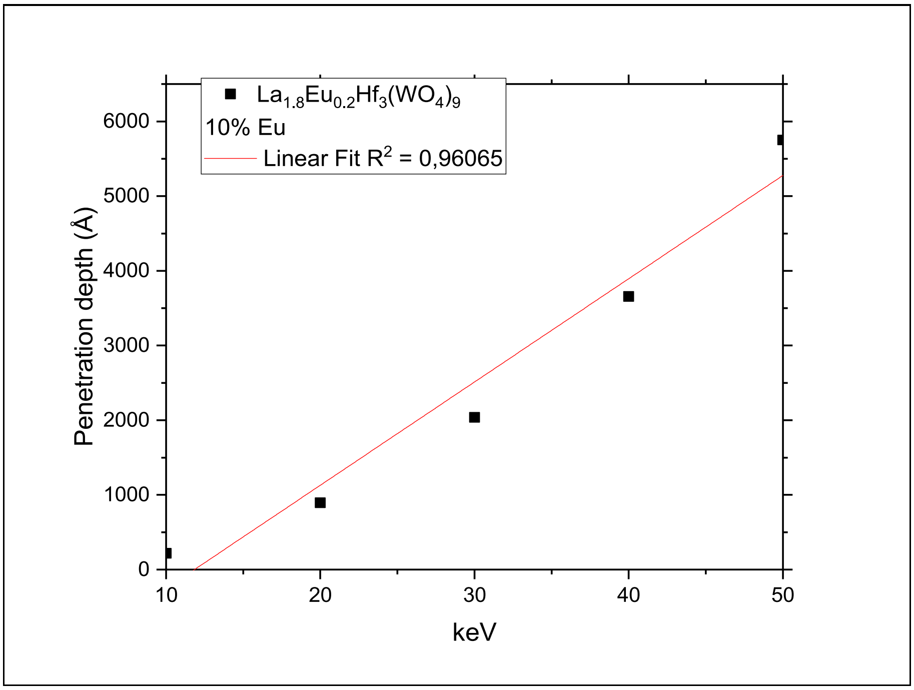

Fig. 9. Calculated approximate values for the X-ray penetration depths by using the Feldman equation.

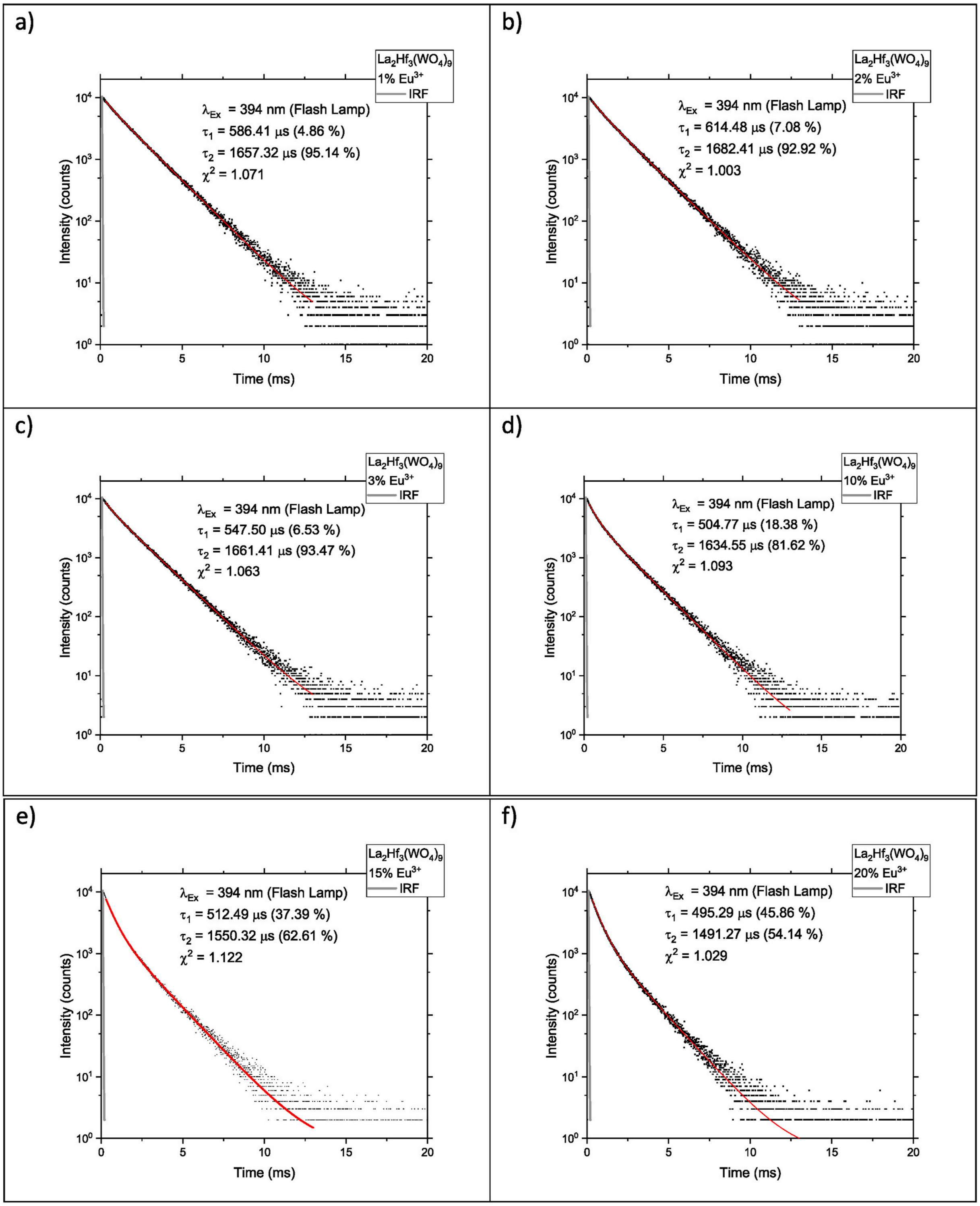

Fig. 10. Decay curves of $La_2Hf_3(WO_4)_9$:Eu^{3+} with a) = 1 % Eu, b) = 2 %, c) = 3 %, d) = 10 %, e) = 15 %, and f) = 20 % Eu^{3+}including the Instrumental Reponse Function.

Table 3
CIE1931 Color coordinates; lumen equivalent for excitation at 394 nm, and the centroid wavelength.

$La_{2-x}Eu_xHf_3(WO_4)_9$ with x=	CIE1931 Color coordinates x; y	Lumen equivalent /$lm \bullet W_{opt}^{-1}$	centroid wavelength nm
0.02	0.6427; 0.3421	213	618.3
0.04	0.6366; 0.3413	216	618.8
0.06	0.6399; 0.3426	215	617.9
0.2	0.6497; 0.3424	217	618.2
0.3	0.6269; 0.3387	219	618.8
0.4	0.6026; 0.3365	222	617.6

Table 4
Color coordinates CIE1931; lumen equivalent for excitation at 160 nm and the centroid wavelength.

$La_{2-x}Eu_xHf3(WO_4)_9$ with x=	CIE1931 Color coordinates x; y	Lumen equivalent /$lm \bullet W_{opt}^{-1}$	centroid wavelength nm
0.02	0.6167; 0.3392	224	619.1
0.04	0.6277; 0.3429	226	619.4
0.06	0.6371; 0.3444	227	618.8
0.2	0.6521; 0.3432	241	618.3
0.3	0.6521; 0.3432	241	618.3
0.4	0.6526; 0.3421	244	618.2

Table 5
CIE1931 color coordinates; lumen equivalent for X-Ray excitation and the centroid wavelength.

$La_{2-x}Eu_xHf_3(WO_4)_9$ with x=	CIE1931 Color coordinates x; y	Lumen equivalent /$lm \bullet W_{opt}^{-1}$	centroid wavelength nm
0.02	0.6396; 0.3492	208	618.6
0.04	0.6389; 0.3486	212	618.2
0.06	0.6420; 0.3483	211	618.8
0.2	0.6429; 0.3486	209	618.3
0.3	0.6265; 0.3485	211	618.2
0.4	0.6168; 0.3495	209	618.2

% Eu^{3+} and is likely associated with Eu^{3+} ions in more isolated regions of the material, where quenching effects are less pronounced. While these observations suggest energy migration and clustering effects, direct evidence for such phenomena remains challenging to obtain, but those assumptions are supported by the results of the reflection spectra. The unreacted WO_3 could lead to the inhomogeneous distribution of dopants. To clarify this assumption, the Instrumental Response Function (IRF) was recorded. The reduced χ^2 values remain close to 1 across all samples, indicating a good fit of the biexponential model to the experimental data.

Lumen equivalents and color coordinates according to CIE1931 were calculated from the emission spectra using the software "Osram Sylvania LED Color Calculator" v4.6 to v7.03 (see Tables 3-5). When excited with 394 nm radiation, the color coordinates show a slight dependence on the Eu^{3+} concentration. From this it can be deduced that the intensity ratios of the different emission lines show slight changes with the Eu^{3+} concentration (Fig. 11).

The calculated chromaticity coordinates (x and y) of the Eu^{3+} doped phosphor provide insights into the color rendering and emission characteristics as a function of Eu^{3+} concentration. Most samples exhibit an x-coordinate around 0.64, which corresponds to the emission of pure red light. However, for the sample with 20 % Eu^{3+}, the x-coordinate shifts to approximately 0.60, indicating a change in the emission color towards an orange-red hue. The y-coordinates remain nearly constant, suggesting that the brightness (luminance) and the blue light contribution are only minimally affected. This shift in the x-coordinate could be attributed to structural changes in the host lattice or variations in the local environment of the Eu^{3+} ions, which influence the electronic transitions and the resulting emission spectrum.

When excited at 160 nm (VUV excitation) or under X-ray excitation, the chromaticity coordinates of the emitted light are very similar and exhibit less variation compared to the coordinates obtained from the emission spectra under 394 nm excitation (Fig. 12). This difference can be understood in the context of the excitation mechanisms and the resulting electronic transitions. At 160 nm or with X-rays, the excitation predominantly involves CT transitions. These transitions corresponds to the excitation of the host material or to transfer energy to the Eu^{3+} ions in a more uniform manner, leading to a consistent emission profile dominated by the intrinsic transitions of Eu^{3+} such as $^5D_0 \rightarrow {}^7F_J$. This results in similar chromaticity coordinates, as the emission is largely governed by the characteristic energy levels of Eu^{3+}. In contrast, excitation at 394 nm directly targets a specific electronic transition of Eu^{3+} ($^7F_0 \rightarrow {}^5L_7$) which may be more sensitive to variations in the local environment of the Eu^{3+} ions. This localized excitation can lead to subtle differences in the emission spectra due to factors such as site symmetry, crystal field effects, or energy transfer interactions, causing greater variation in the chromaticity coordinates. The centroid wavelength of the samples, were calculated with the relative emission integrals consistently around 617–619 nm. This aligns closely with the red region of the visible spectrum. This wavelength corresponds to the characteristic emission of Eu^{3+}, which is primarily associated with the $^5D_0 \rightarrow {}^7F_2$ transition. Its position indicates that the luminescence is perceived as a deep, intense red by the human eye, accurately reflecting the color emitted by Eu^{3+}. The stability of the centroid wavelength across the samples confirms the reliability and purity of the red emission, making it a precise indicator of the visual output of Eu^{3+} based luminescent materials.

4. Conclusions

It turned out, that the Eu^{3+}-doped $La_2Hf_3(WO_4)_9$ solid solutions exhibit remarkable luminescent properties, with concentration-dependent emission intensities and a consistent red emission profile dominated by the $^5D_0 \rightarrow {}^7F_2$ transitions. Under 394 nm excitation, the emission spectra reveal intense, sharp lines at 592.5 nm, 617.5 nm, and 696 nm, attributed to specific Eu^{3+} electronic transitions. The emission intensity steadily increases with Eu^{3+} doping, peaking at 15 %, before quenching effects dominate at higher concentrations. Under X-ray excitation, luminescence peaks at 10 % Eu^{3+} doping, with diminishing efficiency at lower excitation voltages due to reduced penetration depths, as calculated using the Feldman equation. These results underscore the strong red emission and the dependence of luminescent properties on both excitation methods and Eu^{3+} concentration. However, the material's low thermal stability ($T_{1/2} = 228$ K) and quenching behavior at higher concentrations highlight its limitations for high-temperature applications. The study provides comprehensive insights into the luminescent behavior of Eu^{3+}-activated $La_2Hf_3(WO_4)_9$, emphasizing its potential in specific luminescent applications, such as optical marking, temperature sensing, or scintillation.

CRediT authorship contribution statement

Julia Goldmann: Writing – original draft, Visualization, Investigation. **Tim Pier:** Project administration, Investigation. **Thomas Jüstel:** Supervision, Resources, Conceptualization.

Declaration of competing interest

The authors declare that they have no known competing financial interests or personal relationships that could have appeared to influence the work reported in this paper.

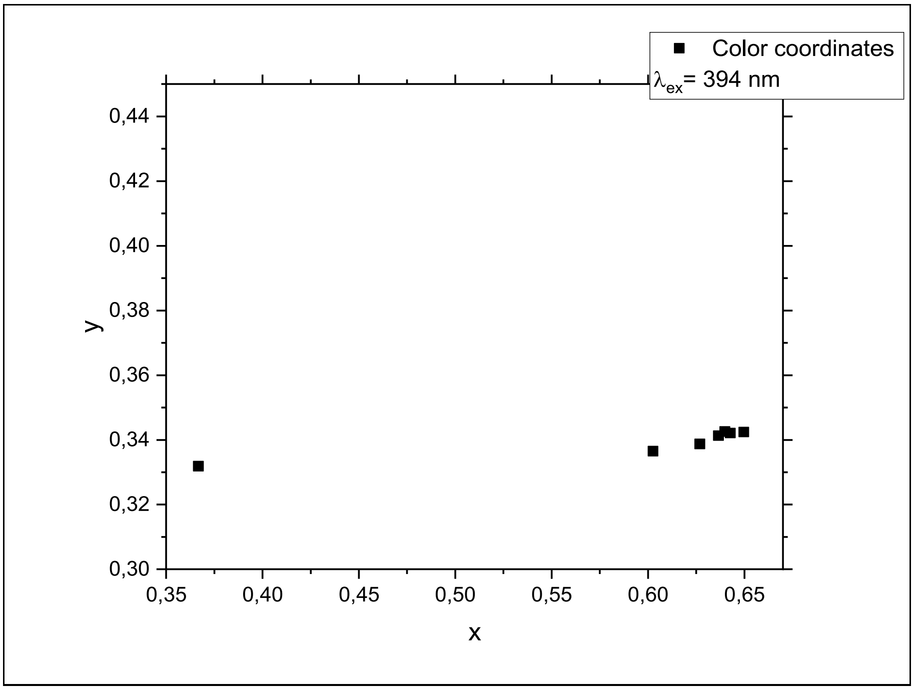

Fig. 11. CIE1931 color coordinates of $La_{2-x}Eu_x(WO_4)_9$ at 394 nm excitation.

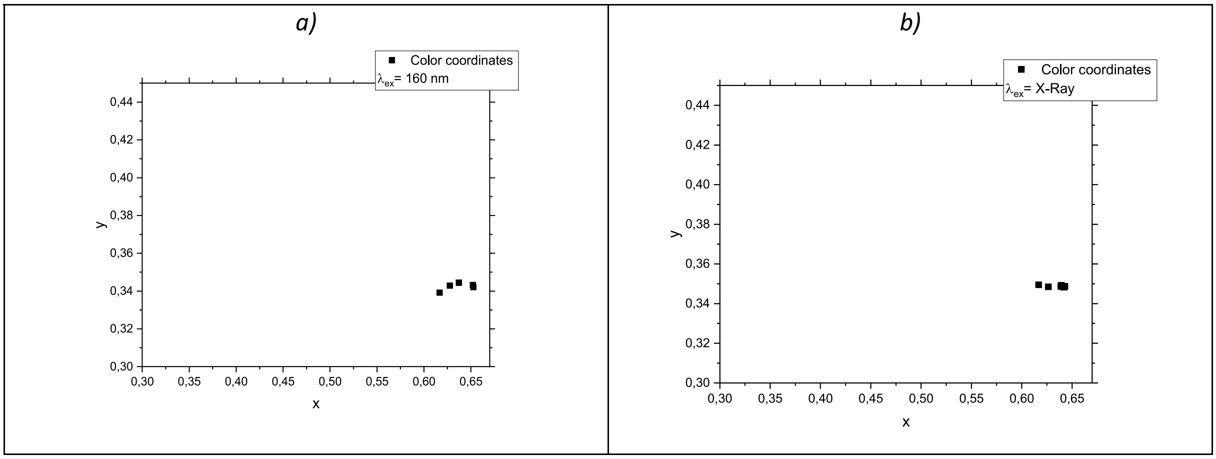

Fig. 12. a) CIE1931 color coordinates of $La_{2-x}Eu_x(WO_4)_9$ at 160 nm excitation; b) CIE1931 color coordinates of $La_{2-x}Eu_x(WO_4)_9$ at X-Ray excitation. (For interpretation of the references to color in this figure legend, the reader is referred to the Web version of this article.)

Acknowledgements

The authors are grateful to the state of North Rhine Westphalia, Germany for financial support.

Data availability

Data will be made available on request.

References

[1] H.J. Borchardt, Rare-Earth phosphors, J. Chem. Phys. 38 (1963) 1251, https://doi.org/10.1063/1.1733830.

[2] A.M. Kaczmarek, R. van Deun, Rare earth tungstate and molybdate compounds - from 0D to 3D architectures, Chem. Soc. Rev. 42 (2013) 8835–8848, https://doi.org/10.1039/C3CS60166H.

[3] Le Han, J. Liu, P. Liu, B. Li, X. Li, Y. Xu, Dual-emissive Eu3+, Tb3+ co-doped Gd2 (MoO4)3 phosphor for optical thermometry application, J. Phys. Chem. Solid. 153 (2021) 110032, https://doi.org/10.1016/j.jpcs.2021.110032.

[4] Y. Zeng, Z. Li, L. Wang, Y. Xiong, Controlled synthesis of Gd2(WO4)3 microstructures and their tunable photoluminescent properties after Eu3+/Tb3+ doping, CrystEngComm 14 (2012) 7043, https://doi.org/10.1039/C2CE26077H.

[5] R. Ma, C. Ma, J. Zhang, J. Long, Z. Wen, X. Yuan, Y. Cao, Energy transfer properties and enhanced color rendering index of chromaticity tunable green-yellow-red-emitting Y_3Al_5O_12: Ce^3+, Cr^3+ phosphors for white light-emitting diodes, Opt. Mater. Express 7 (2017) 454, https://doi.org/10.1364/ome.7.000454.

[6] J. Chen, G. Wu, J. Tang, B. Xu, P. Liu, X. Sun, Optimization of general and special color rendering index with red quantum dots for white LEDs, in: 2021 4th International Conference on Advanced Electronic Materials, Computers and Software Engineering (AEMCSE), IEEE, Changsha, China, 2021, pp. 1203–1206.

[7] Y. Narukawa, M. Ichikawa, D. Sanga, M. Sano, T. Mukai, White light emitting diodes with super-high luminous efficacy, J. Phys. D Appl. Phys. 43 (2010) 354002, https://doi.org/10.1088/0022-3727/43/35/354002.

[8] A.M. Srivastava, T.F. Soules, Phosphors, in: Kirk-Othmer Encyclopedia of Chemical Technology, Wiley, 2001.

[9] K. Binnemans, Interpretation of europium(III) spectra, Coord. Chem. Rev. 295 (2015) 1–45, https://doi.org/10.1016/j.ccr.2015.02.015.

[10] A.M. Srivastava, T.J. Sommerer, Fluorescent lamp phosphors, Electrochem. Soc. Interface 7 (1998) 28–31, https://doi.org/10.1149/2.F06982IF.

[11] A.A. Setlur, Phosphors for LED-based solid-state lighting, Electrochem. Soc. Interface (2009) 32.

[12] R. Mueller-Mach, G. Mueller, M.R. Krames, H.A. Höppe, F. Stadler, W. Schnick, T. Juestel, P. Schmidt, Highly efficient all-nitride phosphor-converted white light emitting diode, Phys. Status Solidi 202 (2005) 1727–1732, https://doi.org/10.1002/PSSA.200520045.

[13] F. Baur, F. Glocker, T. Jüstel, Photoluminescence and energy transfer rates and efficiencies in Eu 3+ activated Tb 2 Mo 3 O 12, J. Mater. Chem. C 3 (2015) 2054–2064, https://doi.org/10.1039/C4TC02588A.

[14] W. Wang, P. Zhu, Red photoluminescent Eu3+-doped Y2O3 nanospheres for LED-phosphor applications: synthesis and characterization, Opt Express 26 (2018) 34820–34829, https://doi.org/10.1364/OE.26.034820.

[15] S. Som, S. Das, S. Dutta, H.G. Visser, M.K. Pandey, P. Kumar, R.K. Dubey, S. K. Sharma, Synthesis of strong red emitting Y 2 O 3 :Eu 3+ phosphor by potential chemical routes: comparative investigations on the structural evolutions, photometric properties and Judd–Ofelt analysis, RSC Adv. 5 (2015) 70887–70898, https://doi.org/10.1039/C5RA13247A.

[16] Y.-N. Xu, Z. Gu, W.Y. Ching, Electronic, structural, and optical properties of crystalline yttria, Phys. Rev. B 56 (1997) 14993–15000, https://doi.org/10.1103/PhysRevB.56.14993.

[17] L.E. Shea, J. McKittrick, O.A. Lopez, E. Sluzky, Synthesis of red-emitting, small particle size luminescent oxides using an optimized combustion process, J. Am. Ceram. Soc. 79 (1996) 3257–3265, https://doi.org/10.1111/j.1151-2916.1996.tb08103.x.

[18] J. Dhanaraj, R. Jagannathan, T.R.N. Kutty, C.-H. Lu, Photoluminescence characteristics of Y 2 O 3 :Eu 3+ nanophosphors prepared using Sol−Gel thermolysis, J. Phys. Chem. B 105 (2001) 11098–11105, https://doi.org/10.1021/jp0119330.

[19] G.A. Hirata, J. McKittrick, M. Avalos-Borja, J.M. Siqueiros, D. Devlin, Physical properties of Y2O3:Eu luminescent films grown by MOCVD and laser ablation, Appl. Surf. Sci. 113–114 (1997) 509–514, https://doi.org/10.1016/S0169-4332(96)00829-X.

[20] W. Liu, R. Zuo, A novel low-temperature firable La2Zr3(MoO4)9 microwave dielectric ceramic, J. Eur. Ceram. Soc. 38 (2018) 339–342, https://doi.org/10.1016/j.jeurceramsoc.2017.08.023.

[21] L. Shi, C. Liu, H. Zhang, R. Peng, G. Wang, X. Shi, X. Wang, W. Wang, Crystal structure, Raman spectroscopy, metal compatibility and microwave dielectric properties of Ce2Zr3(MoO4)9 ceramics, Mater. Chem. Phys. 250 (2020) 122954, https://doi.org/10.1016/j.matchemphys.2020.122954.

[22] J. Zheng, C. Xing, Y. Yang, S. Li, H. Wu, Z. Wang, Structure, infrared reflectivity spectra and microwave dielectric properties of a low-firing microwave dielectric ceramic Pr2Zr3(MoO4)9, J. Alloys Compd. 826 (2020) 153893, https://doi.org/10.1016/j.jallcom.2020.153893.

[23] X. Ma, C. Li, Z. Fan, H. Wu, Y. Zhang, Z. Zhang, Crystal structure, infrared spectra, and microwave dielectric properties of low-firing Nd2Zr3(MoO4)9 ceramics prepared by reaction-sintering process, J. Mater. Sci. Mater. Electron. 31 (2020) 12620–12627, https://doi.org/10.1007/s10854-020-03812-x.

[24] Y.H. Zhang, J.J. Sun, N. Dai, Z.C. Wu, H.T. Wu, C.H. Yang, Crystal structure, infrared spectra and microwave dielectric properties of novel extra low-temperature fired Eu2Zr3(MoO4)9 ceramics, J. Eur. Ceram. Soc. 39 (2019) 1127–1131, https://doi.org/10.1016/j.jeurceramsoc.2018.12.042.

[25] C.F. Xing, B. Wu, J. Bao, H.T. Wu, Y.Y. Zhou, Crystal structure, infrared spectra and microwave dielectric properties of a novel low-firing Gd2Zr3(MoO4)9 ceramic, Ceram. Int. 45 (2019) 22207–22214, https://doi.org/10.1016/J.CERAMINT.2019.07.243.

[26] Z.G. Bazarova, E.Y. Badmaeva, S.F. Solodovnikov, Y.L. Tushinova, B.G. Bazarov, E. S. Zolotova, Russ. J. Inorg. Chem. (2004) 284.

[27] L. Vegard, Die Konstitution der Mischkristalle und die Raumfllung der Atome, Z. Phys. 5 (1921) 17–26, https://doi.org/10.1007/BF01349680.

[28] G. Li, H. Chai, Q. Yang, Y. Wei, Enhanced luminescence properties of Eu3+ activated CaGd2(WO4)4 red-emitting phosphors with Mo6+ doping, J. Mater. Sci. Mater. Electron. 30 (2019) 9200–9210, https://doi.org/10.1007/s10854-019-01249-5.

[29] C.-H. Chiu, M.-F. Wang, C.-S. Lee, T.-M. Chen, Structural, spectroscopic and photoluminescence studies of LiEu(WO4)2−x(MoO4)x as a near-UV convertible phosphor, J. Solid State Chem. 180 (2007) 619–627, https://doi.org/10.1016/j.jssc.2006.11.015.

[30] L. Li, W. Chang, J. He, Y. Yan, M. Cui, S. Jiang, G. Xiang, X. Zhou, Molybdenum substitution simultaneously induced band structure modulation and luminescence enhancement in LiLaMg(W, Mo)O6: Eu3+ red-emitting phosphor for near ultraviolet excited white light diodes, J. Alloys Compd. 763 (2018) 278–288, https://doi.org/10.1016/j.jallcom.2018.05.306.

[31] A.M. Abakumov, V.A. Morozov, A.A. Tsirlin, J. Verbeeck, J. Hadermann, Cation ordering and flexibility of the BO_4^{2-} tetrahedra in incommensurately modulated $CaEu_2(BO_4)_4$ (B = Mo, W) scheelites, Inorg. Chem. 53 (2014) 9407–9415, https://doi.org/10.1021/ic5015412.

[32] R.D. Shannon, Revised effective ionic radii and systematic studies of interatomic distances in halides and chalcogenides, Acta Crystallogr. A 32 (1976) 751–767, https://doi.org/10.1107/S0567739476001551.

[33] F. Baur, T. Jüstel, New red-emitting phosphor La2Zr3(MoO4)9:Eu3+ and the influence of host absorption on its luminescence efficiency, Aust. J. Chem. 68 (2015) 1727, https://doi.org/10.1071/CH15268.

[34] G. Blasse, B.C. Grabmaier, Luminescent Materials, 1994.

[35] K.K. Rasu, D. Balaji, S.M. Babu, Spectroscopic properties of Eu 3+ :KLa(WO 4) 2 novel red phosphors, J. Lumin. 170 (2016) 547–555, https://doi.org/10.1016/j.jlumin.2015.10.006.

[36] A. Nayak K. Goswami, A. Gosh, R. Debnath, Luminescence efficiency of Eu+3 in Y2O3: the effect of reduction of particle size and incorporation of trace hetero-cations in the Y2O3 lattice, Indian J, Pure Appl. Phys. (2009) 775–781.

[37] M. Kottaisamy, K. Horikawa, H. Kominami, T. Aoki, N. Azuma, T. Nakamura, Y. Nakanishi, Y. Hatanaka, Synthesis and characterization of fine particle Y[sub 2]O[sub 2]S:Eu red phosphor at low-voltage excitation, J. Electrochem. Soc. 147 (2000) 1612, https://doi.org/10.1149/1.1393405.

[38] D. Boyer, G. Bertrand-Chadeyron, R. Mahiou, C. Caperaa, J.-C. Cousseins, Synthesis dependent luminescence efficiency in Eu3+ doped polycrystalline YBO3, J. Mater. Chem. 9 (1999) 211–214, https://doi.org/10.1039/a804514c.

[39] F.C. Palilla, A.K. Levine, YVO(4):Eu: a highly efficient, red-emitting phosphor for high pressure mercury lamps, Appl. Opt. 5 (1966) 1467–1468, https://doi.org/10.1364/AO.5.001467.

[40] M. Janulevicius, P. Marmokas, M. Misevicius, J. Grigorjevaite, L. Mikoliunaite, S. Sakirzanovas, A. Katelnikovas, Luminescence and luminescence quenching of highly efficient Y2Mo4O15:Eu(3+) phosphors and ceramics, Sci. Rep. 6 (2016) 26098, https://doi.org/10.1038/srep26098.

[41] L. Wang, Z. Liu, Z. Chen, D. Zhao, G. Qin, W. Qin, Upconversion emissions from high-energy states of Eu3+ sensitized by Yb3+ and Ho3+ in β-NaYF4 microcrystals under 980 nm excitation, Opt Express 19 (2011) 25471–25478, https://doi.org/10.1364/OE.19.025471.

[42] D. Pi, F. Wang, X. Fan, M. Wang, Y. Zhang, Luminescence behavior of Eu3+ doped LaF3 nanoparticles, Spectrochim. Acta Mol. Biomol. Spectrosc. 61 (2005) 2455–2459, https://doi.org/10.1016/j.saa.2004.09.009.

[43] B. Tian, B. Chen, Y. Tian, X. Li, J. Zhang, J. Sun, H. Zhong, L. Cheng, S. Fu, H. Zhong, Y. Wang, X. Zhang, H. Xia, R. Hua, Excitation pathway and temperature dependent luminescence in color tunable Ba5Gd8Zn4O21:Eu3+ phosphors, J. Mater. Chem. C 1 (2013) 2338, https://doi.org/10.1039/C3TC00915G.

[44] M. Müller, T. Jüstel, Energy transfer and unusual decay behaviour of BaCa2Si3O9: Eu(2+),Mn(2+) phosphor, Dalton Trans. 44 (2015) 10368–10376, https://doi.org/10.1039/C5DT00591D.

[45] G. Blasse, Thermal quenching of characteristic fluorescence, J. Chem. Phys. 51 (1969) 3529–3530, https://doi.org/10.1063/1.1672543.

[46] C. Feldman, Range of 1-10 kev electrons in solids, Phys. Rev. 117 (1960) 455–459, https://doi.org/10.1103/PhysRev.117.455.